Supplementary Information

Theoretical Roadmap for Best Oxygen Reduction Activity in Two-dimensional Transition Metal Tellurides

Xin Yang,[a,b] Hanyu Liu,[a,b,c,d] Zexing Qu,[e] Yu Xie,[*a,b,c] and Yanming Ma[a,b,d]

[a]State Key Laboratory of Superhard Materials, College of Physics, Jilin University, Changchun 130012, China

[b]International Center of Computational Method and Software, College of Physics, Jilin University, Changchun 130012, China

[c]Key Laboratory of Physics and Technology for Advanced Batteries (Ministry of Education), College of Physics, Jilin University, Changchun 130012, China

[d]International Center of Future Science, Jilin University, Changchun 130012, China

[e]Institute of Theoretical Chemistry, College of Chemistry, Jilin University, Changchun, 130023, China

Corresponding author: Yu Xie

E-mail address: xieyu@jlu.edu.cn

This file includes:
- Methods
- Geometric and Electronic Properties (Figure S1-2)
- Origin of O_2 activation (Figure S3-11)
- ORR catalytic performance and linear scaling (Figure S12-18)
- Rational screening of activity descriptor (Figure S19-27)
- Supplementary Tables (Table S1-7)
- References

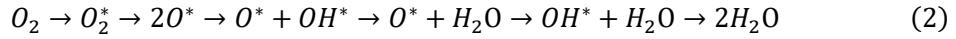# Methods

Computational details

Density functional theory computations were performed by using the Vienna *Ab initio* simulation package (VASP) within the projected augmented wave method.[1, 2] The Brillouin zone was sampled using k-points of 4×4×1 for the supercell with a×b of around 10 Å×10 Å.[3] For some monolayers with a×b of around 20 Å×10 Å, such as Ta$_4$Pd$_3$Te$_{16}$, the *k*-points were sampled using 2×4 ×1. The *p*-band center (ε_p) of the Te sites was calculated by

$$\varepsilon_p = \frac{\int_{-\infty}^{0} \varepsilon \rho_p(\varepsilon) d\varepsilon}{\int_{-\infty}^{0} \rho_p(\varepsilon) d\varepsilon} \tag{1}$$

where $\rho_p(\varepsilon)$ is the *p*-band density of states of a Te atom and ε is the energy of electrons.

ORR Reactions

The 4e$^-$ dissociative and associative mechanism pathways for ORR are generally the following equations (2) and (3), respectively.[4] Here, * denotes an adsorption site of the catalyst.

$$O_2 \rightarrow O_2^* \rightarrow 2O^* \rightarrow O^* + OH^* \rightarrow O^* + H_2O \rightarrow OH^* + H_2O \rightarrow 2H_2O \tag{2}$$

$$O_2 \rightarrow O_2^* \rightarrow OOH^* \rightarrow O^* + H_2O \rightarrow OH^* + H_2O \rightarrow 2H_2O \tag{3}$$

The free energy of each species can be expressed using the equation:

$$G = E_{DFT} + E_{ZPE} + \int C_p dT - TS \tag{4}$$

where E_{DFT}, E_{ZPE} and S are the ground state electronic energy, zero-point vibrational energy and entropy, respectively. The values of E_{ZPE} and S of intermediates are obtained from frequency calculations and the values for molecules are taken from the NIST database (Computational Chemistry Comparison and Benchmark Database), which are listed in Table S6. T is the temperature of 298.15 K. Solvent effects have been considered by using the Poissson-Boltzmann implicit solvation model.[5] The dielectric constant ε is taken as 80 for water. The absorption free energy for the adsorbates can be calculated using the equation:

$$\Delta G_{ads} = \Delta E_{ads} + \Delta E_{ZPE} - T\Delta S \tag{5}$$

where ΔG_{ads} is the adsorption free energy of adsorbates, and ΔE_{ZPE} and ΔS are the difference of E_{ZPE} and S, respectively. The free energy of O_2 was computed by the equation:

$$G_{O_2} = 2G_{H_2O} - 2G_{H_2} - 4.92 \ eV \tag{6}$$

The calculation of energy in volcano plots

The free energies for the four steps in dissociative mechanism can be defined as:

$$\Delta G_1 = G_{(O+OH)^*} - G_{(O+O)^*} - G_{(H^+ + e^-)} = \Delta G_{(O+OH)^*} - \Delta G_{(O+O)^*} \tag{7}$$

$$\Delta G_2 = G_{O^*} + G_{H_2O} - G_{(O+OH)^*} - G_{(H^+ + e^-)} = \Delta G_{O^*} - \Delta G_{(O+OH)^*} \tag{8}$$

$$\Delta G_3 = G_{OH^*} - G_{O^*} - G_{(H^+ + e^-)} = \Delta G_{OH^*} - \Delta G_{O^*} \tag{9}$$

$$\Delta G_4 = G_* + G_{H_2O} - G_{OH^*} - G_{(H^+ + e^-)} = -\Delta G_{OH^*} \tag{10}$$

The relations between OH and other adsorbates can be used to define the limiting potentials in dissociative mechanism as a function of the OH adsorption energy as:

$$U_{L1} = -\Delta G_1 = -\ 0.2 \ \Delta G_{OH^*} + 1.6 \tag{11}$$

$$U_{L2} = -\Delta G_2 = 1.7\Delta G_{OH^*} - 0.6 \tag{12}$$

$$U_{L3} = -\Delta G_3 = -1.2\Delta G_{OH^*} + 2.1 \tag{13}$$

$$U_{L4} = -\Delta G_4 = \Delta G_{OH^*} \tag{14}$$

The free energies for the four steps in associative mechanism can be defined as:

$$\Delta G_1 = G_{OOH*} - G_{O_2} - G_* - G_{(H^+ + e^-)} = \Delta G_{OOH*} - 4.92 \tag{15}$$

$$\Delta G_2 = G_{O*} + G_{H_2O} - G_{OOH*} - G_{(H^+ + e^-)} = \Delta G_{O*} - \Delta G_{OOH*} \tag{16}$$

$$\Delta G_3 = G_{OH*} - G_{O*} - G_{(H^+ + e^-)} = \Delta G_{OH*} - \Delta G_{O*} \tag{17}$$

$$\Delta G_4 = G_* + G_{H_2O} - G_{OH*} - G_{(H^+ + e^-)} = -\Delta G_{OH*} \tag{18}$$

The relations between OH and other adsorbates can be used to define the limiting potentials in associative mechanism as a function of the OH adsorption energy as:

$$U_{L1} = -\Delta G_1 = -\Delta G_{OH*} + 1.6 \tag{19}$$

$$U_{L2} = -\Delta G_2 = 1.2 \ \Delta G_{OH*} + 1.2 \tag{20}$$

$$U_{L3} = -\Delta G_3 = -1.2 \ \Delta G_{OH*} + 2.1 \tag{21}$$

$$U_{L4} = -\Delta G_4 = \Delta G_{OH*} \tag{22}$$

The above equations result in four limiting potential lines for the four elementary steps, which could form the volcano plot.

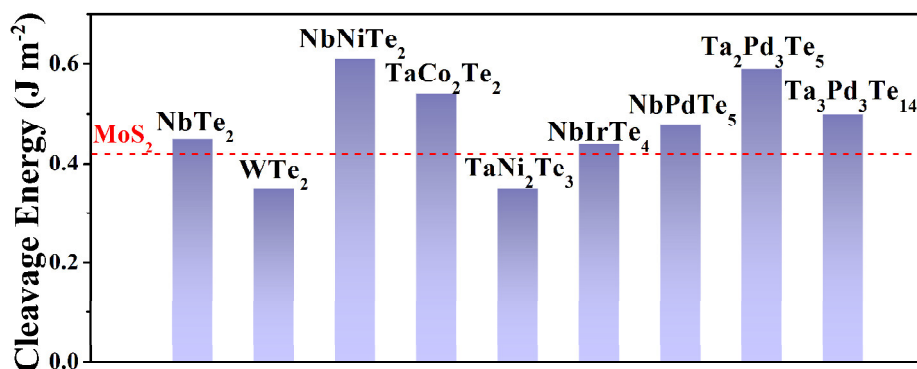# Geometric and Electronic Properties

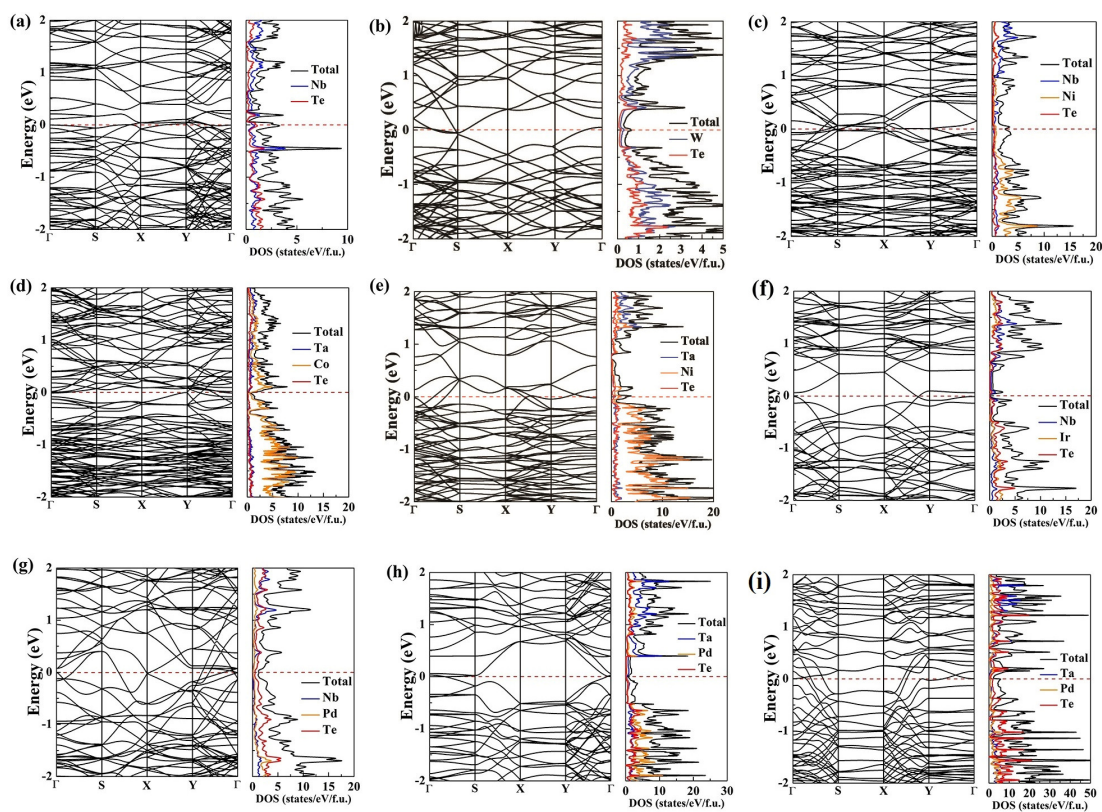**Figure S1**. The calculated cleavage energies of studied 9 monolayer tellurides.

Figure S2. Band structure and density of states (DOS) of monolayer (a) $NbTe_2$, (b) WTe_2, (c) $NbNiTe_2$, (d) $TaCo_2Te_2$, (e) $TaNi_2Te_3$, (f) $NbIrTe_4$, (g) $NbPdTe_5$, (h) $Ta_2Pd_3Te_5$, and (i) $Ta_3Pd_3Te_{14}$. $NbIrTe_4$ is semi-metallic with zero band-gap and others are metallic.

Origin of O₂ activation

The O_2 adsorption configurations, energy barriers of O_2 dissociation, and the analysis of underlying O_2 adsorption mechanism are shown in this part.
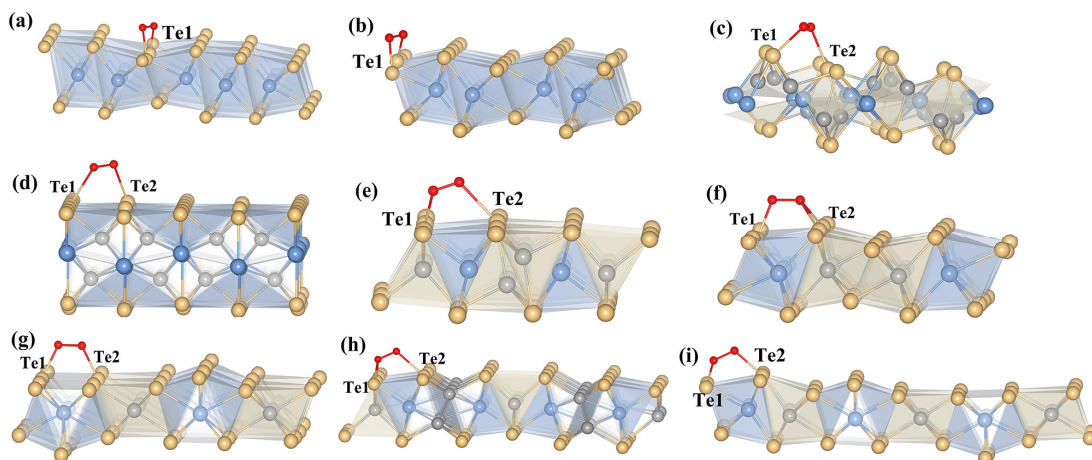

Figure S3. The O_2 adsorption configurations of (a) $NbTe_2$, (b) WTe_2, (c) $NbNiTe_2$, (d) $TaCo_2Te_2$, (e) $TaNi_2Te_3$, (f) $NbIrTe_4$, (g) $NbPdTe_5$, (h) $Ta_2Pd_3Te_5$, and (i) $Ta_3Pd_3Te_{14}$.
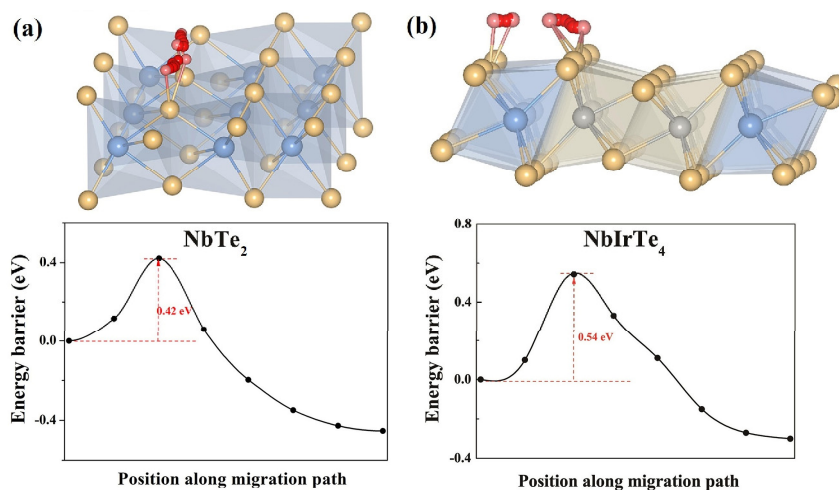

Figure S4. The energy barriers of O_2 dissociation in monolayer (a) $NbTe_2$ and (b) $NbIrTe_4$ from NEB calculations.
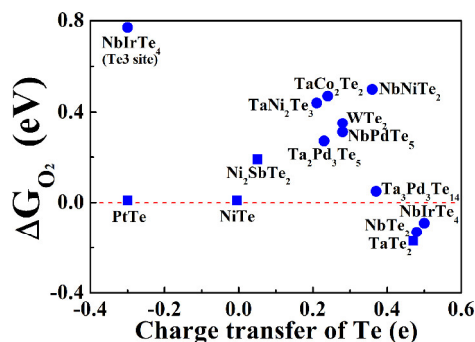

Figure S5. The O_2 adsorption energy of studied tellurides versus charge transfer. The Te active sites are Te1 atoms that mainly interact with O_2 with stronger bonding strength. The previous studied tellurides $PtTe$, $NiTe$, $TaTe_2$, and Ni_2SbTe_2 have also been considered for comparison.[6-9] Notably, the O_2 adsorption energy of NiTe was recalculated in this study and the details of the calculation of NiTe are shown in Table S7.
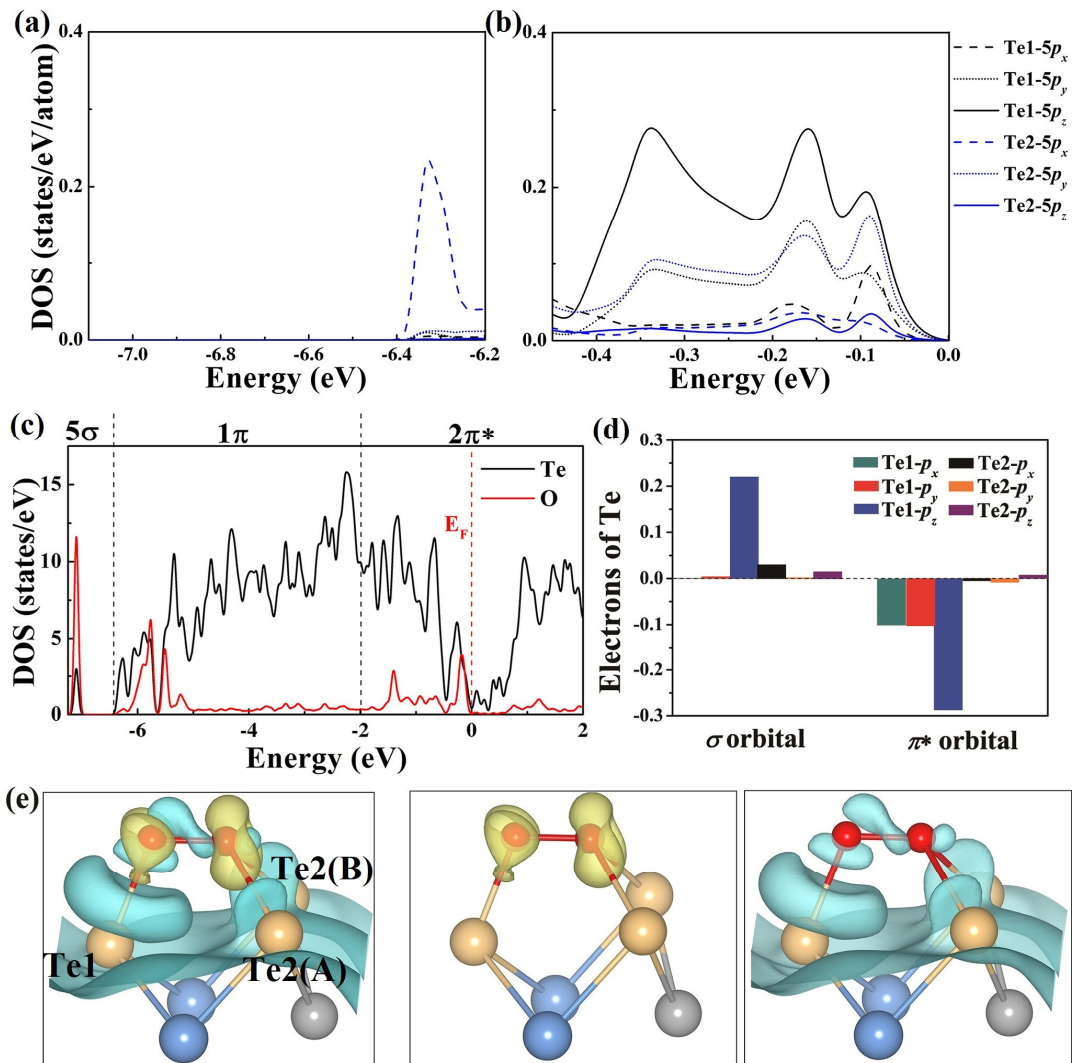
Figure S6. pDOS of Te1 and Te2 atoms in NbIrTe$_4$ (a) from -7.2 to -6.2 eV and (b) from -0.2 to 0 eV. (c) DOS of Te and O elements with orbitals of O$_2$ marked on the top and (d) integrated electrons of the difference of pDOS of Te1 and Te2 between NbIrTe$_4$ and O$_2$-adsorpted NbIrTe$_4$. Notably, the orbitals here are O$_2$ that has adsorbed on NbIrTe$_4$. (e) Differential charge density distributions of O$_2$ adsorbed NbIrTe$_4$.
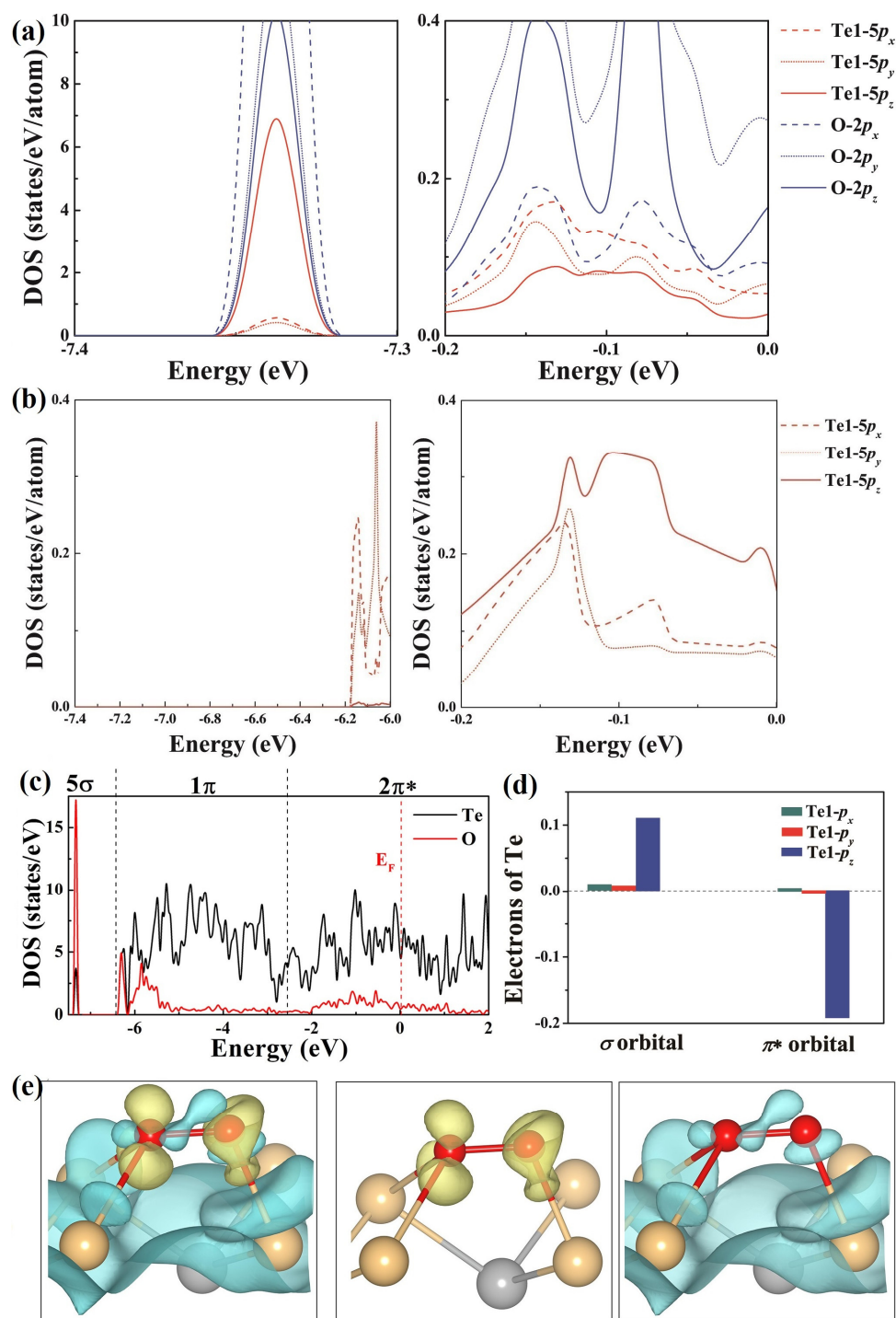
Figure S7. (a) pDOS of Te1 and O atoms in O₂ adsorpted PtTe and (b) Te atoms in PtTe. (c) DOS of Te and O elements with orbitals of O₂ marked on the top (d) integrated electrons of the difference of pDOS between PtTe and O₂ adsorbed PtTe. Notably, the orbitals here are O₂ that has adsorbed on PtTe. (e) Differential Charge density distributions of O₂ on PtTe monolayer.
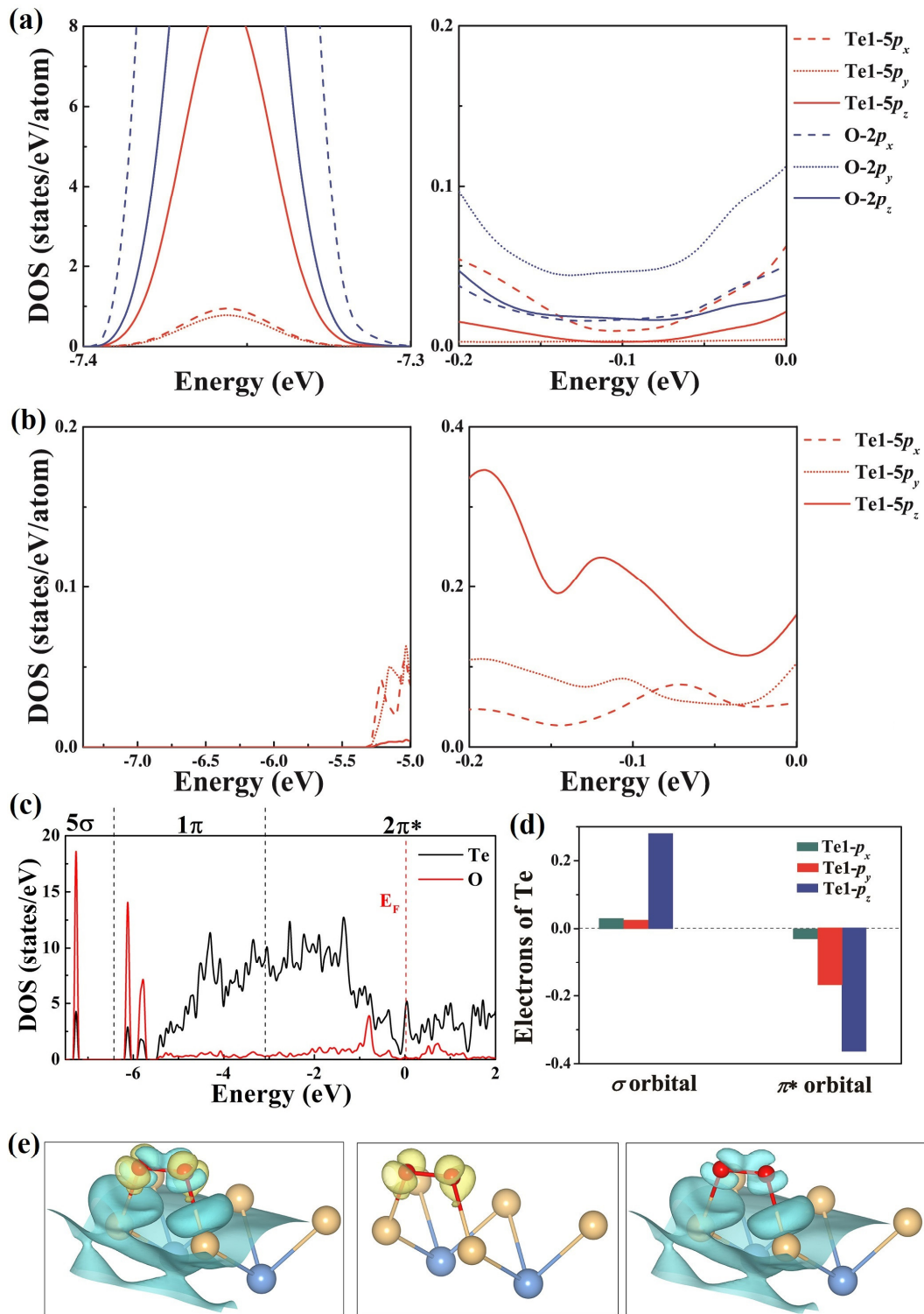
Figure S8. (a) pDOS of Te1 and O atoms in O_2 adsorpted $NbTe_2$ and (b) Te atoms in $NbTe_2$. (c) DOS of Te and O elements with orbitals of O_2 marked on the top (d) integrated electrons of the difference of pDOS between $NbTe_2$ and O_2 adsorbed $NbTe_2$. Notably, the orbitals here are O_2 that has adsorbed on $NbTe_2$. (e) Differential Charge density distributions of O_2 on $NbTe_2$ monolayer.
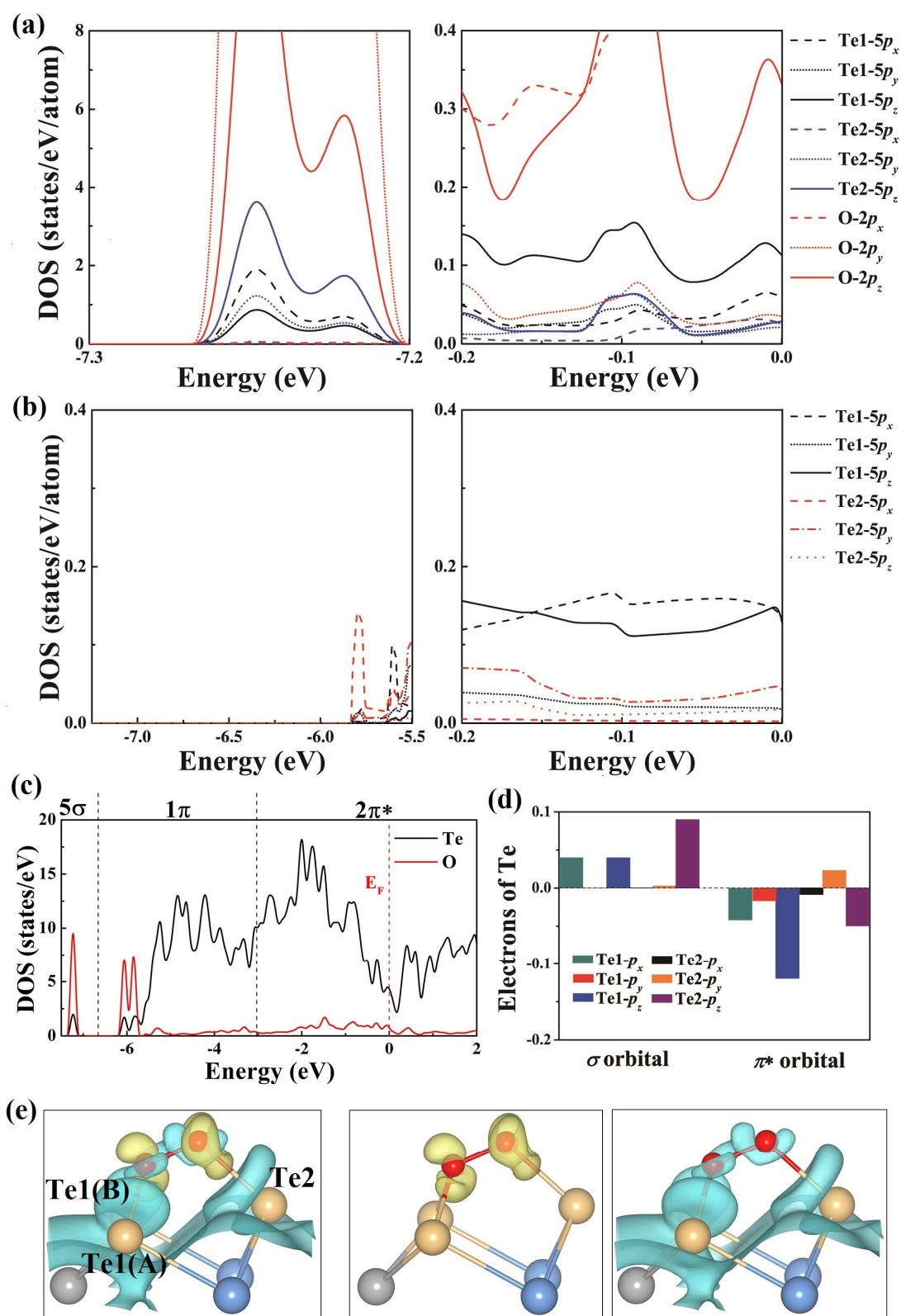
Figure S9. (a) pDOS of Te1, Te2 and O atoms in O$_2$-adsorpted Ta$_3$Pd$_3$Te$_{14}$ and (b) Ta$_3$Pd$_3$Te$_{14}$. (c) DOS of Te and O elements with orbitals of O$_2$ marked on the top (d) integrated electrons of the difference of pDOS between Ta$_3$Pd$_3$Te$_{14}$ and O$_2$-adsorbed Ta$_3$Pd$_3$Te$_{14}$. Notably, the orbitals here are O$_2$ that has adsorbed on Ta$_3$Pd$_3$Te$_{14}$. (e) Differential Charge density distributions of O$_2$ on Ta$_3$Pd$_3$Te$_{14}$ monolayer.
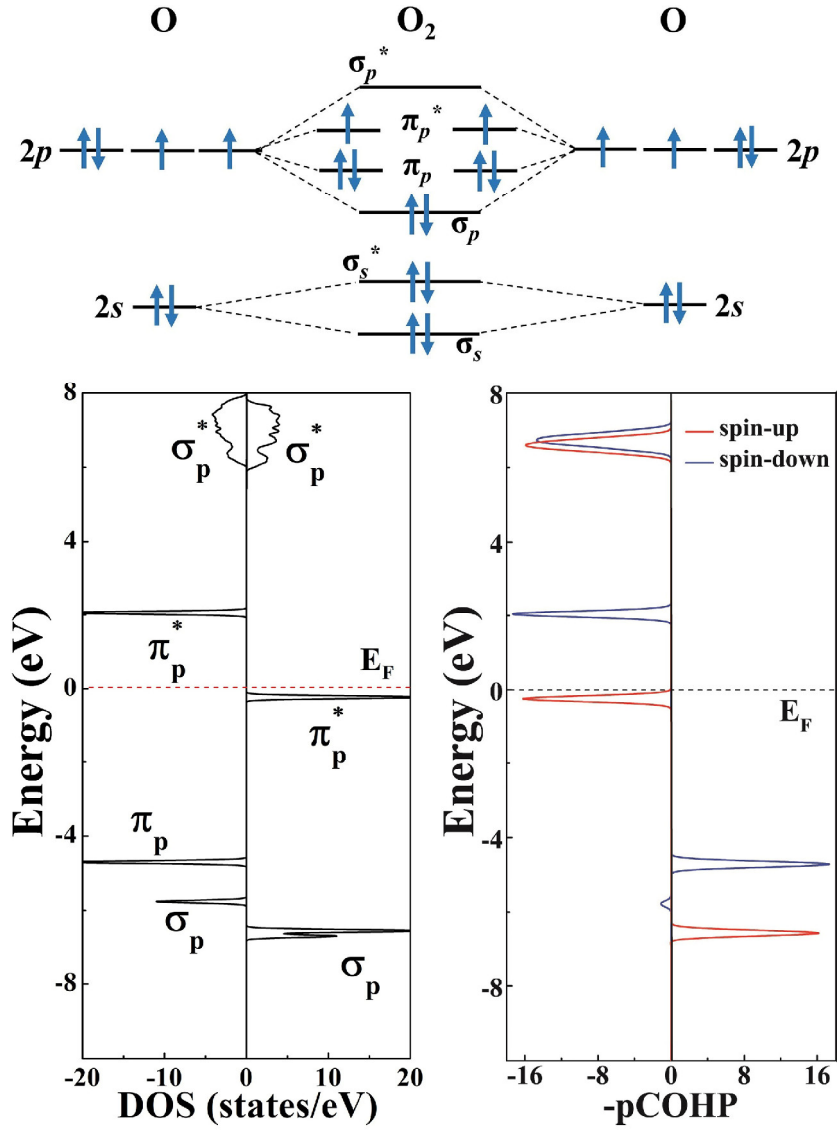
Figure S10. Schematic representation for O_2 molecule and calculated DOS and pCOHP curves.
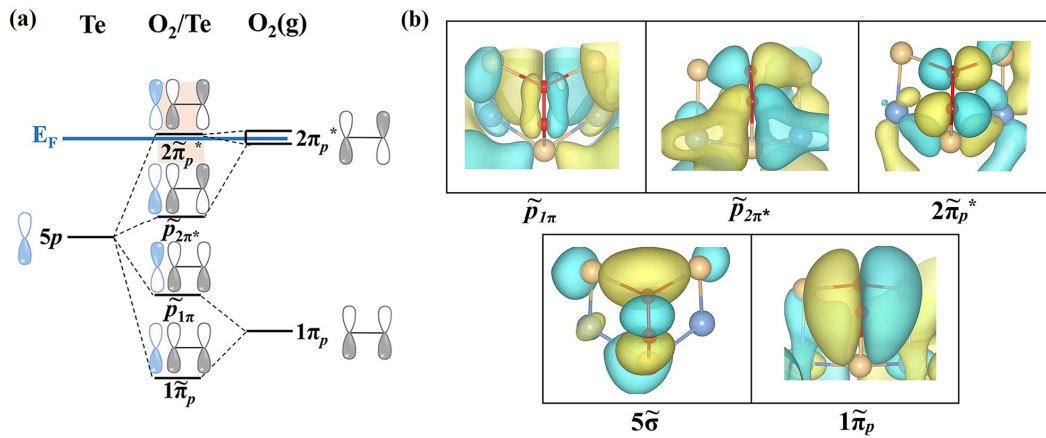

Figure S11. (a) Schematic representation of π interactions and (b) the $5\tilde{\sigma}$, $1\tilde{\pi}_p$, $\tilde{p}_{1\pi}$, $\tilde{p}_{2\pi*}$, and $2\tilde{\pi}_p*$ orbitals for O_2 adsorbed on NbIrTe$_4$. Notably, $5\tilde{\sigma}$ contributes to the "donation" and $\tilde{p}_{2\pi*}$ and $2\tilde{\pi}_p*$ contributes to "back-donation" process.

ORR catalytic performance and linear scaling

The configurations and the free energy diagrams for monolayer $NbTe_2$, $NbIrTe_4$, and $Ta_3Pd_3Te_{14}$, the structural, electronic, and catalytic properties of $NbIrTe_4$ multilayers, and the relationship between ΔG_{O*} and ΔG_{OH*} are shown in this part.
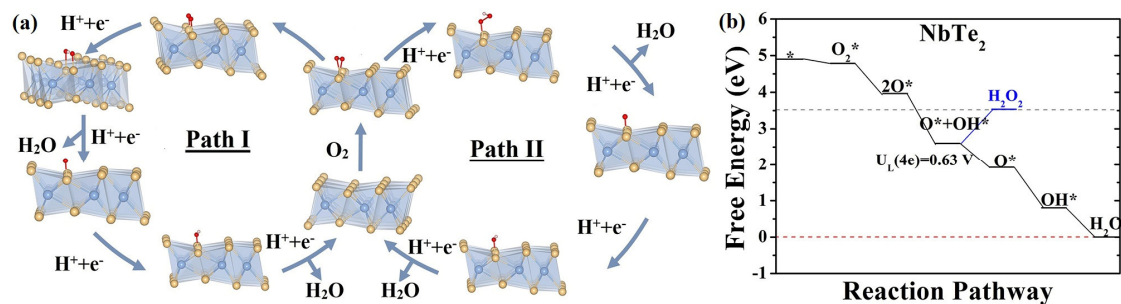
Figure S12. (a) Scheme of the possible two ORR reaction pathways and (b) free energy diagram for the associative ORR pathway on monolayer $NbTe_2$.
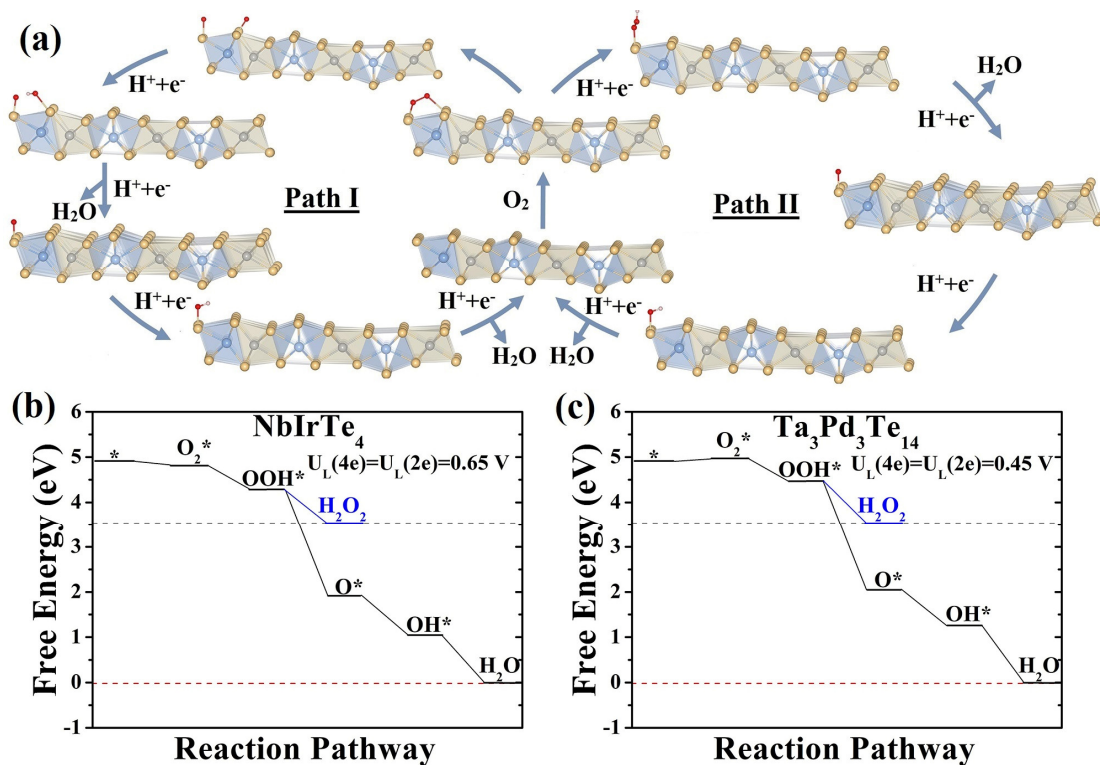
Figure S13. (a) Scheme of the possible two ORR reaction pathways monolayer $Ta_3Pd_3Te_{14}$. and free energy diagrams for the associative ORR pathway on monolayer (b) $NbIrTe_4$ and (c) $Ta_3Pd_3Te_{14}$ at U=0 V.
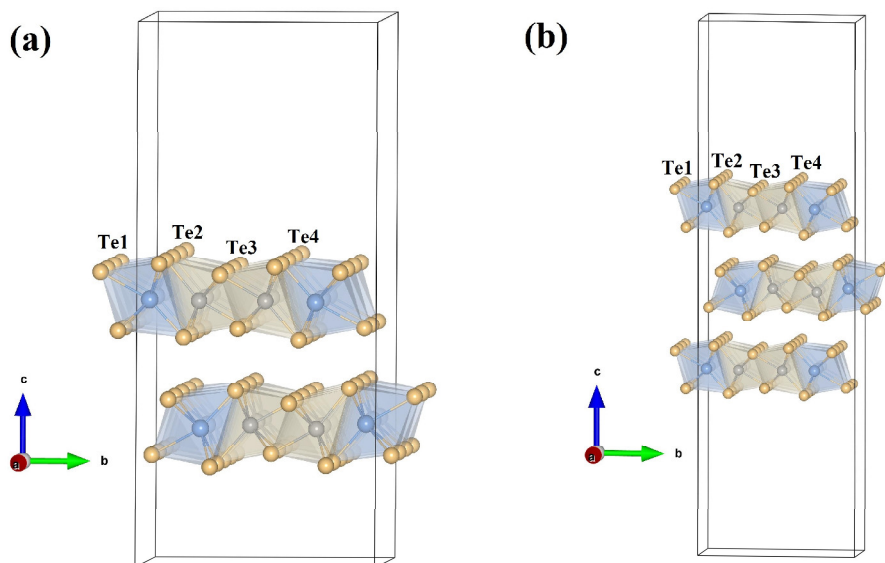
Figure S14. The structures of (a) bilayer and (b) trilayer NbIrTe$_4$.
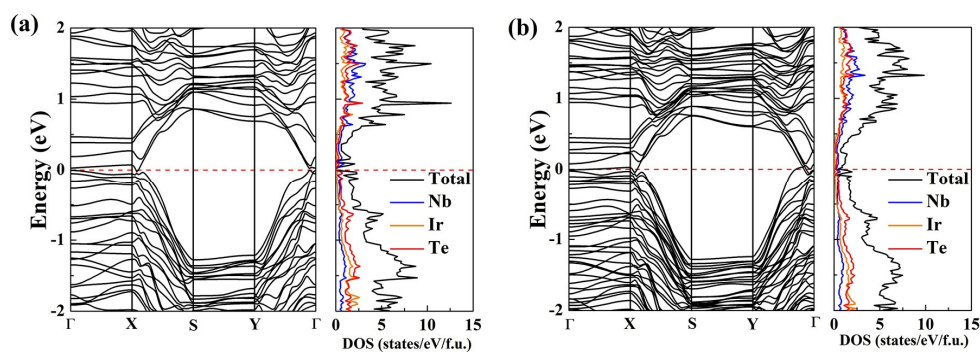
Figure S15. Band structure and density of states (DOS) of (a) bilayer and (b) trilayer NbIrTe$_4$.
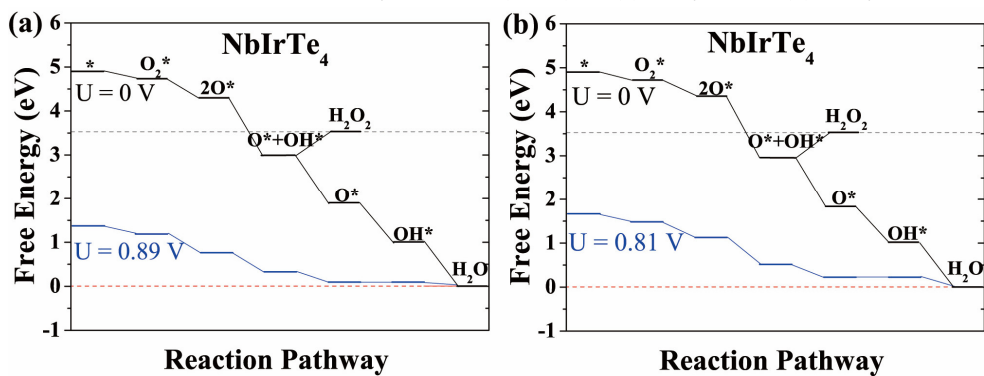
Figure S16. Free energy diagrams for the dissociative ORR pathway on (a) bilayer and (b) trilayer NbIrTe$_4$.
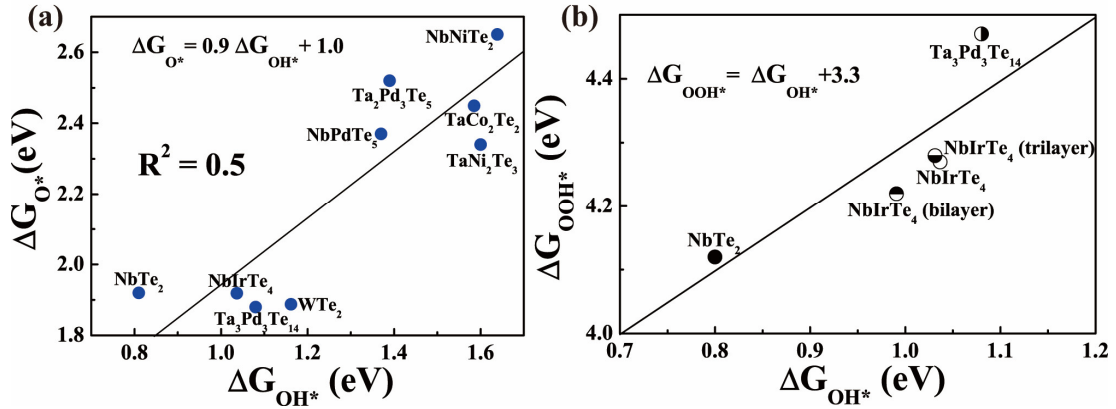
Figure S17. (a) The Variation of ΔG_O* versus $\Delta G_{OH}*$ in studied 9 tellurides. (b) Variation of ΔG_{OOH*} as a function of $\Delta G_{OH}*$ in newly found promising telluride catalysts. We here determined the limiting potentials: $U_L = \min\{-\Delta G_1, -\Delta G_2, -\Delta G_3, -\Delta G_4\}$, where ΔG_1, ΔG_2, ΔG_3, and ΔG_4 are the free energy of four reaction steps. With the scaling relations between OH* and other adsorbates, the limiting potential of dissociation pathway can be given by equation:

$$U_L = \min\{-0.2\ \Delta G_{OH^*} + 1.2, 1.9\ \Delta G_{OH^*} - 0.9, -1.3\ \Delta G_{OH^*} + 2.2, \Delta G_{OH^*}\}$$

Thus the estimated highest limiting potentials for dissociation pathway is 0.94 V.
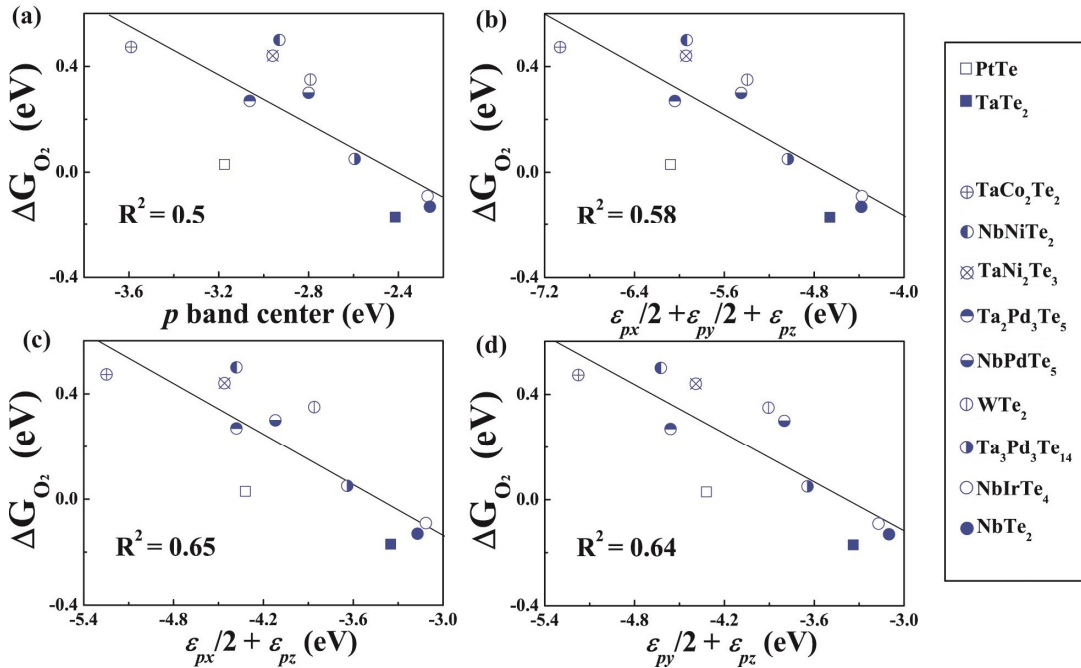
Figure S18. O_2 adsorption energy versus other considered descriptors of (a) p band center, (b) ε_{px} /2 + ε_{px} /2 + ε_{px} /2, (c) ε_{px} /2 + ε_{px} /2, and (d) ε_{px} /2 + ε_{px} /2, where ε_{px}, ε_{py}, and ε_{pz} defines centroid of the projected density of states of the p_x, p_y, and p_z orbitals relative to the Fermi level. The correlation coefficient R^2 of other descriptors are smaller than that of ε_{pz}.

Rational screening of activity descriptor

The calculated cleavage energies and ORR pathways of newly studied monolayer tellurides, and the analysis of the adsorption energies of oxygen-containing groups are shown here.

(a)

(b)
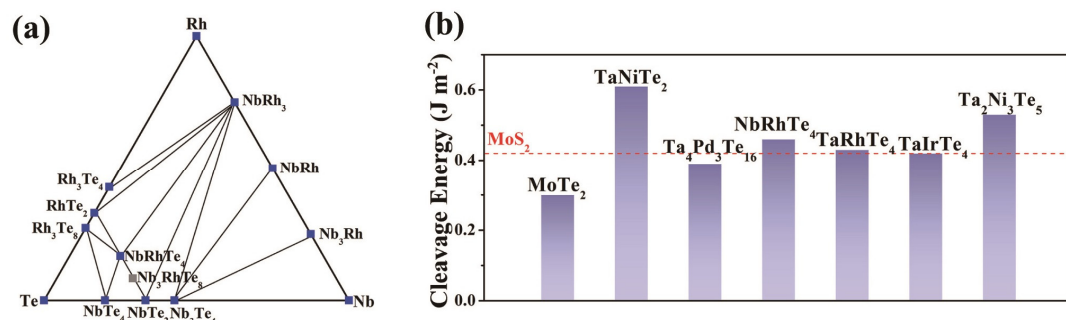
Figure S19. (a) The calculated cleavage energies of newly studied monolayer tellurides. (b) The calculated phase diagram of Nb-Rh-Te system.
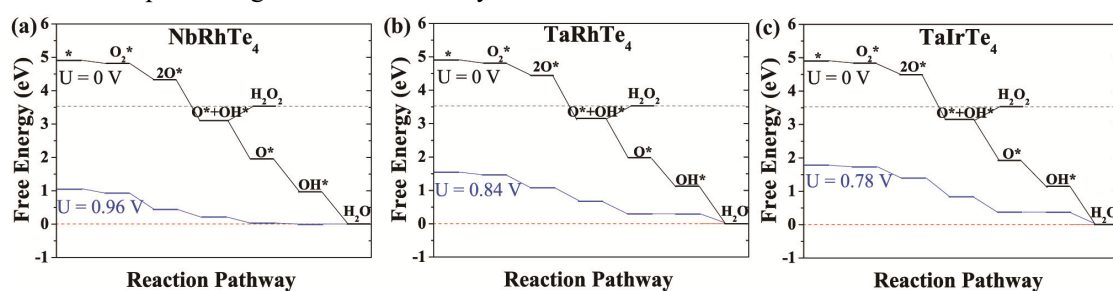
Figure S20. Free energy diagrams for the dissociative ORR pathway on monolayer (a) NbRhTe$_4$, (b) TaRhTe$_4$, and (c) TaIrTe$_4$.
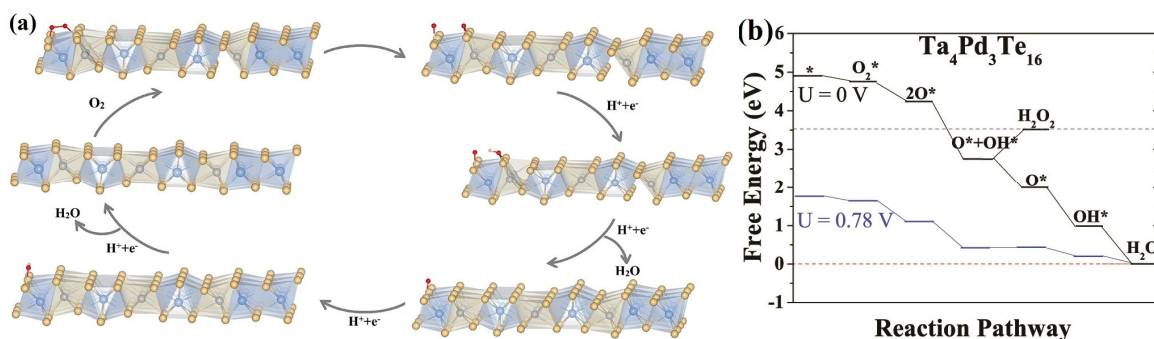
Figure S21. (a) Scheme of the dissociation reaction pathway and (b) free energy diagrams for the dissociative ORR pathway on monolayer Ta$_4$Pd$_3$Te$_{16}$.
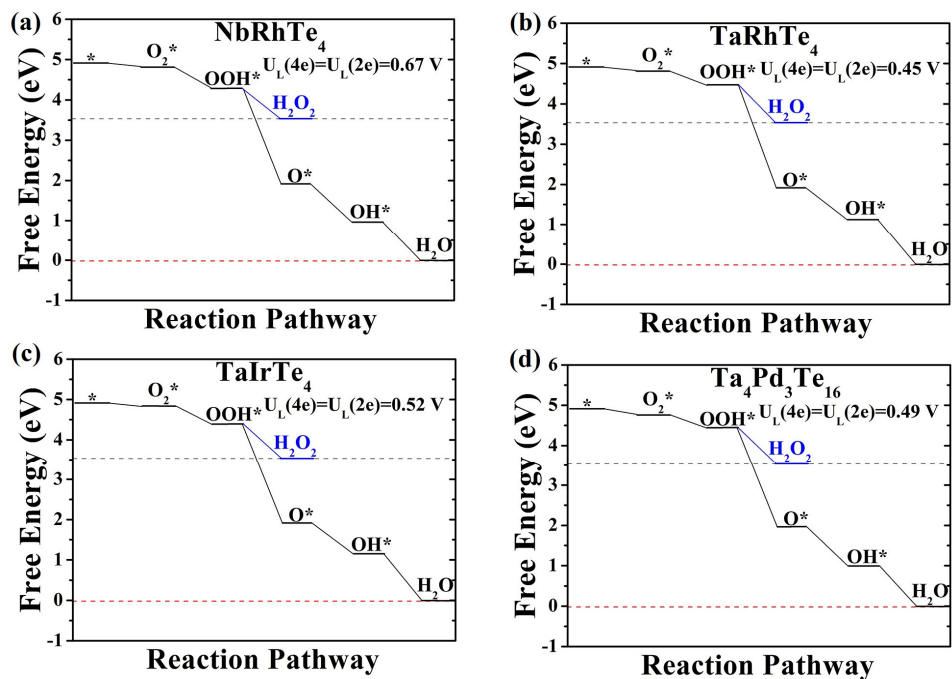
Figure S22. Free energy diagrams for the associative ORR pathway on monolayer (a) NbRhTe$_4$, (b) TaRhTe$_4$, (c) TaIrTe$_4$, and (d) Ta$_4$Pd$_3$Te$_{16}$.
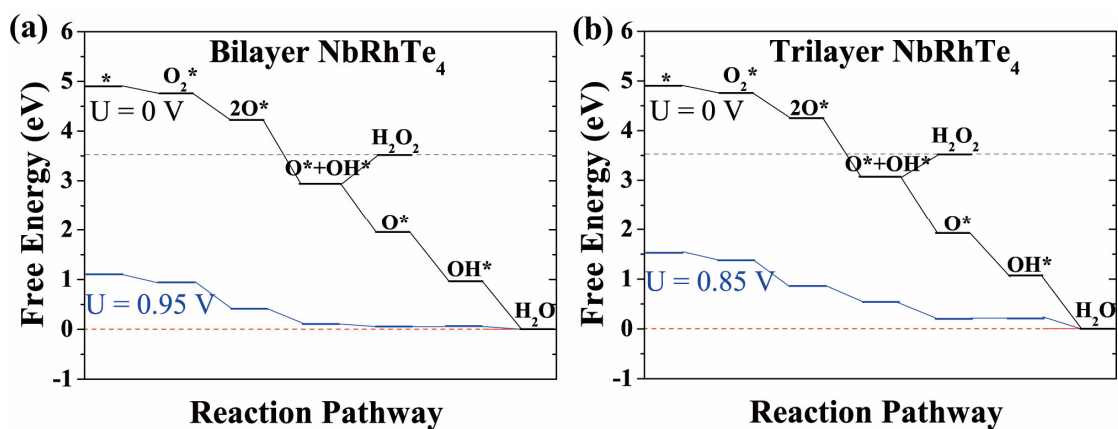
Figure S23. Free energy diagrams for the dissociative ORR pathway on (a) bilayer and (b) trilayer NbRhTe$_4$.
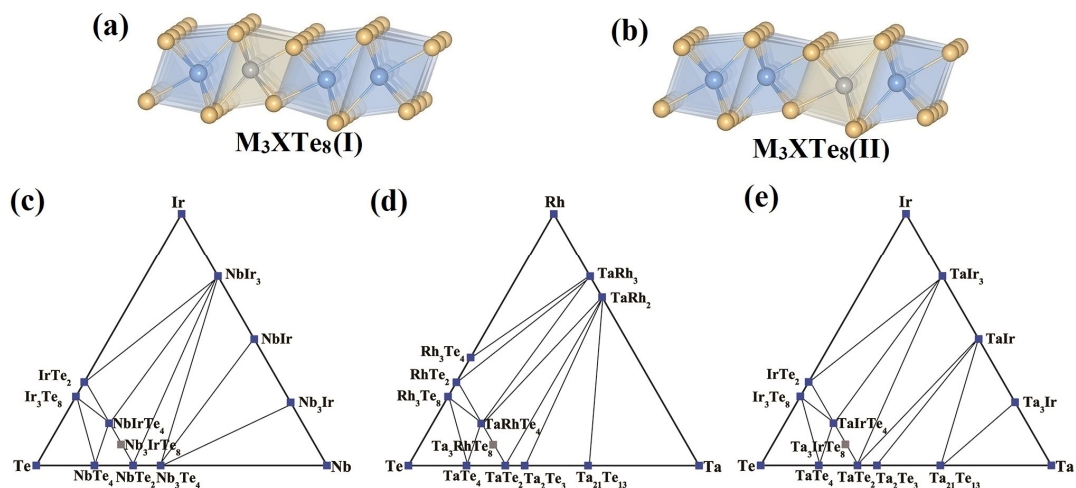
Figure S24. The structures of (a) $M_3XTe_8(I)$ and (b) $M_3XTe_8(II)$ and the phase diagrams of (c) Nb-Ir-Te, (d) Ta-Rh-Te, and (e) Ta-Ir-Te systems. The calculated formation energies of the bulk phases of hypothetic Nb_3RhTe_8, Nb_3IrTe_8, Ta_3RhTe_8, Ta_3IrTe_8 were 20, 24, 20, and 25 meV/atom, respectively. The phase diagram of Nb-Rh-Te system was shown in Figure S19.
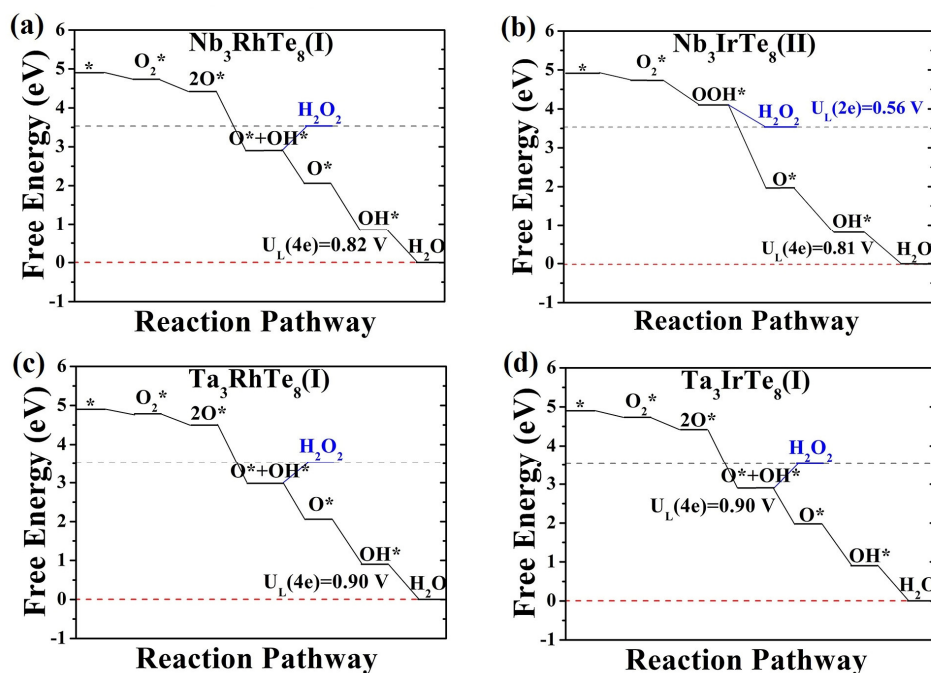
Figure S25. Free energy diagrams for the dissociative ORR pathway on monolayer (a) $Nb_3RhTe_8(I)$, (c) $Ta_3RhTe_8(I)$ and (d) $Ta_3IrTe_8(I)$ and the associative ORR pathway on monolayer (b) $Nb_3IrTe_8(II)$.
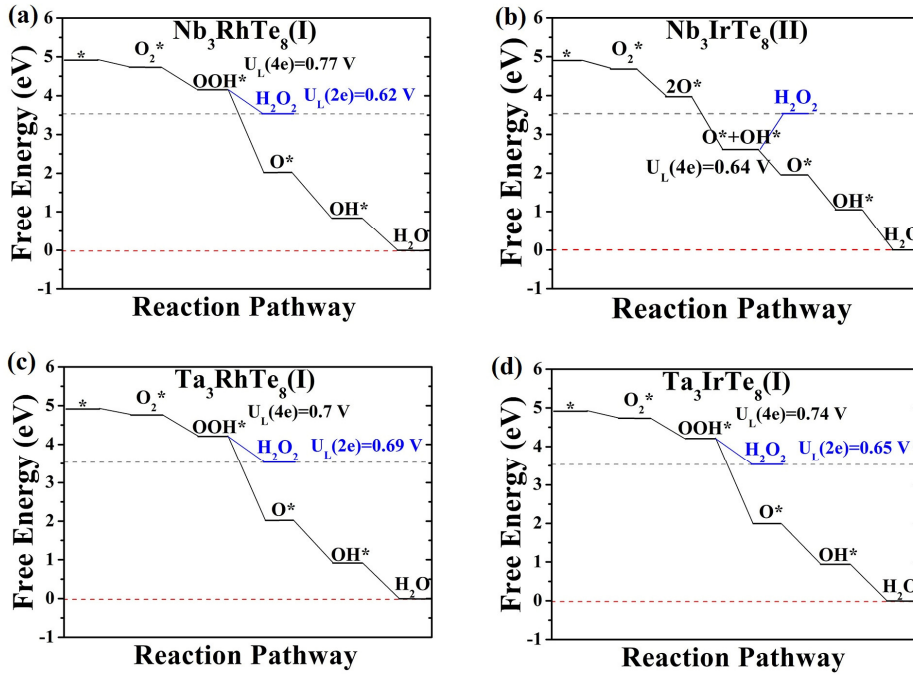
Figure S26. Free energy diagrams for the associative ORR pathway on monolayer (a) $Nb_3RhTe_8(I)$, (c) $Ta_3RhTe_8(I)$ and (d) $Ta_3IrTe_8(I)$ and the dissociative pathway on monolayer (b) $Nb_3IrTe_8(II)$.
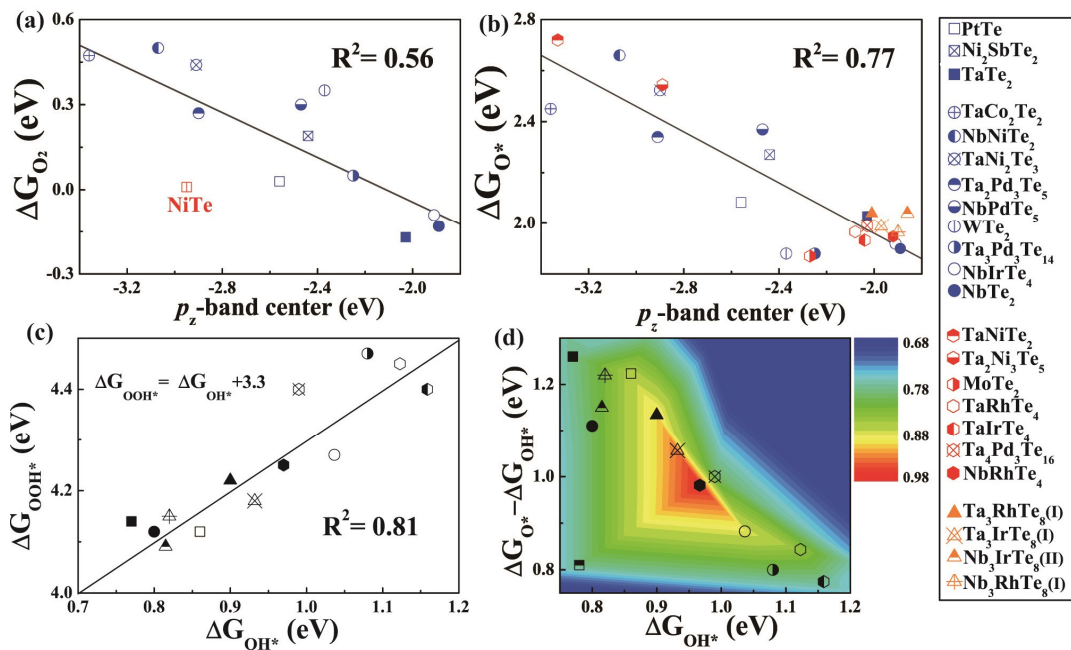
Figure S27. (a) O_2 adsorption energy versus the average p_z-band center of Te atoms for initially studied tellurides. Notably, the ΔG_{O_2} of NiTe was recalculated in this study and the details of the calculation are shown in Table S7. The ΔG_{O_2} of NiTe can't accord with the linear relationship, which might attract more attention in subsequent study. (b) The ΔG_O versus the p_z-band center of active Te sites for all studied tellurides. (c)Variation of ΔG_{OOH*} as a function of $\Delta G_{OH}*$ for monolayer tellurides. (d) Catalytic activity of the materials as a function of intermediates formation free energies ΔG_{O*} - ΔG_{OH*} and ΔG_{OH*}. The circle, star, triangle, and square points represent initially-studied tellurides, newly-studied tellurides, M-doped variants, and known catalysts in other studies, respectively.

Table S1. Bader charge calculation results of charge transfer in monolayer tellurides.

	M (e)	X (e)	Te1 (e)	Te2 (e)	Te3 (e)	Te4 (e)	Te5 (e)	Te6 (e)	Te7 (e)	Te8 (e)
NbTe$_2$	-0.95		0.48	0.5	0.5					
WTe$_2$	-0.48		0.28	0.19						
NbNiTe$_2$	-1.03	0.29	0.36	0.37						
TaCo$_2$Te$_2$	-1.12	0.4	0.24	0.02	0.12					
TaNi$_2$Te$_3$	-1.15	X1 0.1 X2 0.26	0.32	0.24	0.21					
NbIrTe$_4$	-1.15	0.58	0.50	0.07	-0.29	0.28				
NbPdTe$_5$	-1.14	0.27	0.28	0.21	0.02	0.32	0.02			
Ta$_2$Pd$_3$Te$_5$	-1.22	0.43	0.24	0.23	0.23					
Ta$_3$Pd$_3$Te$_{14}$	-1.15	0.26	0.10	0.37	0.01	0.31	0.07	0.23	0.25	
MoTe$_2$	-0.44		0.25	0.17						
TaNiTe$_2$	-1.01	0.31	0.34	0.35						
Ta$_4$Pd$_3$Te$_{16}$	-1.15	0.29	0.47	0.18	0.21	0.28	0.05	0.31	-0.03	0.35
NbRhTe$_4$	-1.13	0.38	0.49	0.14	-0.24	0.33				
TaRhTe$_4$	-1.12	0.38	0.47	0.15	-0.24	0.32				
TaIrTe$_4$	-1.14	0.60	0.48	0.07	-0.30	0.27				
Ta$_2$Ni$_3$Te$_5$	-1.15	0.22	0.38	0.26	0.33					

Table S2. Bader charge results of charge transfer and bond length of O$_2$-adsorbed tellurides.

Charge	Te1 (e)	Te2 (e)	O$_1$ (e)	O$_2$ (e)
NbTe$_2$	-0.42	-0.41	0.40	0.39
NbIrTe$_4$	-0.56	Te2 (A) -0.15 Te2 (B) -0.14	0.44	0.43
Ta$_3$Pd$_3$Te$_{14}$	Te1 (A) -0.35 Te1 (B) -0.28	-0.33	0.44	0.43
Ta$_4$Pd$_3$Te$_{16}$	-0.53	Te2 (A) -0.28 Te2 (B) -0.12	0.52	0.31
NbRhTe$_4$	-0.54	Te2 (A) -0.25 Te2 (B) -0.18	0.46	0.38
TaRhTe$_4$	-0.55	Te2 (A) -0.25 Te2 (B) -0.19	0.38	0.47
TaIrTe$_4$	-0.57	Te2 (A) -0.20 Te2 (B) -0.18	0.38	0.49

Bond length	Te1-O (Å)	Te2-O (Å)	O$_1$-O$_2$ (Å)
NbTe$_2$	2.22	2.28	1.38
NbIrTe$_4$	2.13	2.56	1.39
Ta$_3$Pd$_3$Te$_{14}$	2.35	2.25	1.37
Ta$_4$Pd$_3$Te$_{16}$	2.15	2.32	1.39
NbRhTe$_4$	2.14	2.43	1.38
TaRhTe$_4$	2.14	2.49	1.39
TaIrTe$_4$	2.13	2.51	1.39

Table S3. The O_2 adsorption energies on different Te sites in studied monolayers

Adsorption energy (eV) Monolayer	Te1	Te2	Te3	Te4	Te5	Te6	Te7	Te8
NbTe$_2$	-0.13	0.92	0.97					
WTe$_2$	0.35	0.87						
NbNiTe$_2$	0.50	0.71						
TaCo$_2$Te$_2$	0.47	1.13	1.08					
TaNi$_2$Te$_3$	0.44	0.65	0.79					
NbIrTe$_4$	-0.09	0.82	0.73	0.94				
NbPdTe$_5$	0.31	0.46	0.42	0.93	0.43			
Ta$_2$Pd$_3$Te$_5$	0.27	0.84	0.91					
Ta$_3$Pd$_3$Te$_{14}$	0.05	0.87	0.75	0.39	0.41	0.82	0.33	
MoTe$_2$	0.27	0.85						
TaNiTe$_2$	0.69	1.09						
Ta$_4$Pd$_3$Te$_{16}$	-0.16	0.19	0.37	0.41	0.43	0.89	0.50	0.67
NbRhTe$_4$	-0.11	0.86	0.52	0.87				
TaRhTe$_4$	-0.07	0.88	0.55	0.89				
TaIrTe$_4$	-0.05	0.95	0.75	0.99				
Ta$_2$Ni$_3$Te$_5$	0.38	0.95	0.98					

Table S4. The free energy of four reaction steps, the limiting potential and corresponding overpotential in dissociation pathway

Monolayer	ΔG1 (eV)	ΔG2 (eV)	ΔG3 (eV)	ΔG4 (eV)	Limiting potential (V)	Overpotential (V)
NbTe$_2$	-1.37	-0.63	-1.11	-0.80	0.63	0.60
NbIrTe$_4$	-1.25	-1.24	-0.88	-1.04	0.88	0.35
Ta$_3$Pd$_3$Te$_{14}$	-1.38	-1.17	-0.80	-1.08	0.80	0.43
NbRhTe$_4$	-1.21	-1.17	-0.98	-0.96	0.96	0.27
TaRhTe$_4$	-1.26	-1.22	-0.84	-1.12	0.84	0.39
TaIrTe$_4$	-1.32	-1.25	-0.78	-1.16	0.78	0.45
Ta$_4$Pd$_3$Te$_{16}$	-1.48	-0.78	-1.00	-0.99	0.78	0.45
Nb$_3$RhTe$_8$(I)	-1.49	-0.86	-1.22	-0.82	0.82	0.41
Nb$_3$RhTe$_8$(II)	-0.96	-0.78	-0.92	-0.83	0.78	0.45
Nb$_3$IrTe$_8$(I)	-1.55	-0.79	-1.18	-0.79	0.79	0.44
Nb$_3$IrTe$_8$(II)	-1.37	-0.64	-1.15	-0.81	0.64	0.59
Ta$_3$RhTe$_8$(I)	-1.52	-0.96	-1.13	-0.90	0.90	0.33
Ta$_3$RhTe$_8$(II)	-1.47	-0.78	-1.25	-0.81	0.78	0.45
Ta$_3$IrTe$_8$(I)	-1.53	-0.90	-1.05	-0.93	0.90	0.33
Ta$_3$IrTe$_8$(II)	-1.28	-0.77	-1.07	-0.88	0.77	0.46

Table S5. The free energy of four reaction steps, the limiting potential and corresponding overpotential in association pathway

Monolayer	$\Delta G1$ (eV)	$\Delta G2$ (eV)	$\Delta G3$ (eV)	$\Delta G4$ (eV)	Limiting potential (V)	Overpotential (V)
NbTe$_2$	-0.80	-2.21	-1.11	-0.80	0.80	0.43
NbIrTe$_4$	-0.65	-2.35	-0.88	-1.04	0.65	0.58
Ta$_3$Pd$_3$Te$_{14}$	-0.45	-2.59	-0.80	-1.08	0.45	0.78
NbRhTe$_4$	-0.67	-2.31	-0.98	-0.96	0.67	0.56
TaRhTe$_4$	-0.45	-2.51	-0.84	-1.12	0.45	0.78
TaIrTe$_4$	-0.52	-2.46	-0.78	-1.16	0.52	0.71
Ta$_4$Pd$_3$Te$_{16}$	-0.49	-2.44	-1.00	-0.99	0.49	0.74
Nb$_3$RhTe$_8$(I)	-0.77	-2.10	-1.22	-0.82	0.77	0.46
Nb$_3$RhTe$_8$(II)	-0.73	-2.44	-0.92	-0.83	0.73	0.50
Nb$_3$IrTe$_8$(I)	-0.98	-1.97	-1.18	-0.79	0.79	0.44
Nb$_3$IrTe$_8$(II)	-0.83	-2.13	-1.15	-0.81	0.81	0.42
Ta$_3$RhTe$_8$(I)	-0.70	-2.19	-1.13	-0.90	0.70	0.53
Ta$_3$RhTe$_8$(II)	-0.79	-2.07	-1.25	-0.81	0.79	0.44
Ta$_3$IrTe$_8$(I)	-0.74	-2.20	-1.05	-0.93	0.74	0.49
Ta$_3$IrTe$_8$(II)	-0.73	-2.24	-1.07	-0.88	0.73	0.50

Table S6. Zero-point energy correction (ΔE_{ZPE}), entropy contribution($T\Delta S$), and total free energy correction (ΔE_{ZPE} - $T\Delta S$) used in the calculations.

Species	ΔE_{ZPE} (eV)	$T\Delta S$ (eV)	ΔE_{ZPE} - $T\Delta S$ (eV)
H$_2$	0.27	0.40	-0.13
H$_2$O	0.56	0.67	-0.11
O$_2$*	0.12	0.16	-0.04
O*	0.06	0.08	-0.02
OH*	0.33	0.13	0.21
OOH*	0.43	0.21	0.22

Table S7. The lattice parameters of bulk NiTe in R-3m phase and the adsorption energy of O$_2$ on monolayer NiTe in different calculations. The results of calculation in solvent model have been used in the above analysis.

	Lattice parameters (Å)
Experimental result[10]	a=b=c=7.04
Theoretical result	a=b=c=7.06
Theoretical result (U=6 eV)	a=b=c=6.93
	Adsorption energy of O$_2$ (eV)
Monolayer NiTe	0.13
Monolayer NiTe (solvent model)	0.01
Monolayer NiTe (solvent model & vdW & U=6 eV)	-0.3

References

1 Wang, Y.; Perdew, J. P., Spin scaling of the electron-gas correlation energy in the high-density limit. *Phys. Rev. B* 1991, **43 (11),** 8911-8916.

2 Kresse, G.; Furthmüller, J., Efficient iterative schemes for ab initio total-energy calculations using a plane-wave basis set. *Phys. Rev. B* 1996, **54 (16),** 11169.

3 Monkhorst, H. J.; Pack, J. D., Special points for Brillouin-zone integrations. *Phys. Rev. B* 1976, **13 (12)**, 5188-5192.

4 Nørskov, J. K.; Rossmeisl, J.; Logadottir, A.; Lindqvist, L.; Kitchin, J. R.; Bligaard, T.; Jónsson, H., Origin of the Overpotential for Oxygen Reduction at a Fuel-Cell Cathode. *J. Phys. Chem. B* 2004, **108 (46)**, 17886-17892.

5 Mathew, K.; Sundararaman, R.; Letchworth-Weaver, K.; Arias, T. A.; Hennig, R. G. *J. Chem. Phys.* 2014, **140,** 084106.

6 Wang, Y.; Li, Y.; Heine, T., PtTe Monolayer: Two-Dimensional Electrocatalyst with High Basal Plane Activity toward Oxygen Reduction Reaction. *J. Am. Chem. Soc.* 2018, **140 (40),** 12732-12735.

7 Wang, Y.; Zhou, K., Two-dimensional metallic tantalum ditelluride with an intrinsic basal-plane activity for oxygen reduction: A microkinetic modeling study. *Green Energy Environ.* 2022, **7 (3),** 525-532.

8 Liu, T.; Wang, Y.; Li, Y., NiTe Monolayer: Two-Dimensional Metal with Superior Basal-Plane Activity for the Oxygen Reduction Reaction. *J. Phys. Chem. C* **2021,** *125* (35), 19164-19170.

9 X Zhao, L.; Yu, G.; Huang, X.; Chen, W., Realizing Efficient Catalytic Performance and High Selectivity for Oxygen Reduction Reaction on a 2D Ni_2SbTe_2 Monolayer. *Inorg. Chem.* 2022, **61 (4),** 2284-2291.

10 Dvoryankina, G. G.; Pinsker, Z. G. A Study of Thin Layers of Phases in the Ni-Te System. A study of the Beta-Phase of NiTe. *Sov. Phys. Crystallogr.* 1964, **8,** 448−451.